Journal of Manufacturing Processes 141 (2025) 556–569

Contents lists available at ScienceDirect

Journal of Manufacturing Processes

journal homepage: www.elsevier.com/locate/manpro

Weldability study of alloys 625 and 718 fabricated by laser-based additive manufacturing

Jhoan Guzman [a,*], Kaue C. Riffel [a], William Evans [b], Eric Brizes [c], Nicholas Avedissian [d], Francisco Werley Cipriano Farias [e,f], Antonio J. Ramirez [a]

[a] Materials Science & Engineering Department, Welding Engineering Program, The Ohio State University, 1248 Arthur E. Adams Dr, Columbus, OH 43221, USA
[b] Metallic Materials and Processes Branch, NASA Marshall Space Flight Center, Huntsville, AL 35812, USA
[c] High Temperature and Smart Alloys Branch, NASA Glenn Research Center, Cleveland, OH 44135, USA
[d] Hexagon Manufacturing Intelligence, North Kingstown, RI, USA
[e] UNIDEMI, Department of Mechanical and Industrial Engineering, NOVA School of Science and Technology, Universidade NOVA de Lisboa, Caparica 2829-516, Portugal
[f] Program of Metallurgical and Materials Engineering, Federal University of Rio de Janeiro (UFRJ), CEP 21941-972 Rio de Janeiro, RJ, Brazil

ARTICLE INFO

Keywords:
Transverse varestraint testing
Directed energy deposition
Laser powder bed fusion
Alloy 718
Alloy 625

ABSTRACT

Nickel-based alloys, Alloys 625 and 718, are widely used in the aerospace industry due to their excellent corrosion resistance and high strength at elevated temperatures. Recently, these alloys have been utilized to manufacture rocket engine components using additive manufacturing (AM) technologies such as laser powder bed fusion (LPBF) and powder-blown laser-based directed energy deposition (DED). These technologies offer faster and more cost-effective production while enabling the fabrication of near-net-shape parts that are subsequently joined by welding. However, solidification cracking susceptibility varies significantly between AM and conventionally processed materials, and limited weldability characterization has been conducted on AM-fabricated materials. This study assesses the weld solidification cracking susceptibility of Alloys 625 and 718 produced by wrought (mill-rolled), LPBF, and DED using transverse varestraint testing, Scheil-Gulliver simulations, the Crack Susceptibility Index (CSI), and the Flow Resistance Index (FRI). Transverse varestraint testing revealed that AM parts exhibited higher susceptibility due to the presence of larger and elongated grains in the fusion zone, affecting the weld solidification cracking response. In Alloy 625, the LPBF condition exhibited the highest maximum crack distance (MCD) of 2.35 ± 0.16 mm, compared to 1.56 ± 0.06 mm for wrought and 1.72 ± 0.10 mm for DED. Similarly, in Alloy 718, the DED condition showed the highest MCD of 2.93 ± 0.41 mm, while the wrought condition had an MCD of 2.01 ± 0.12 mm, and the LPBF condition reached 3.01 ± 0.33 mm at 5 % strain, without a clearly defined saturation strain. Although wrought materials demonstrated greater resistance to solidification cracking, solidification simulations did not correlate with the experimental testing, as they do not account for microstructural and mechanical factors, relying solely on chemistry.

1. Introduction

Nickel (Ni) based alloys are widely used in engineering applications such as aerospace, energy, and nuclear industries, primarily due to their exceptional mechanical properties at both ambient and high temperatures, as well as their high-temperature corrosion resistance [1]. Based on the alloying elements and their respective properties, Ni alloys are classified into several categories: commercially pure Ni alloys, solid-solution-strengthened alloys, precipitation-strengthened alloys, and specialty alloys. Many of these are considered superalloys due to the outstanding performance presented at high temperature. Despite their versality of possible operational conditions, Ni-based superalloys have poor machinability due to their high hardness (even at high temperature), strength, and low thermal conductivity [2].This makes the need to explore wide areas towards improved machining of these alloys. Some opportunities may be found in the different processes routes, such as additive manufacturing (AM), which fabricates net-shape parts (i.e., fewer machining steps) [3,4]. AM technologies offer advantages such as reduced part count, shorter lead times, on-demand fabrication of spare parts, the ability to produce complex geometries, and unique

* Corresponding author.
E-mail addresses: guzmanhernandez.1@osu.edu, jhoanguzmanh@gmail.com (J. Guzman), Ramirez.49@osu.edu (A.J. Ramirez).

https://doi.org/10.1016/j.jmapro.2025.02.051
Received 6 January 2025; Received in revised form 10 February 2025; Accepted 21 February 2025
Available online 8 March 2025
1526-6125/© 2025 The Authors. Published by Elsevier Ltd on behalf of The Society of Manufacturing Engineers. This is an open access article under the CC BY license (http://creativecommons.org/licenses/by/4.0/).

microstructural control [5,6].

Most research on laser powder bed fusion (LPBF) has demonstrated promising results in fabricating low-volume aero-engine components with high precision and complex geometries [6,7]. In recent years, there has been growing interest in using large-scale AM processes to produce free-form, large components that require longer printing times or are simply not feasible to manufacture using LPBF due to the size limitations of the build chamber. Beyond powder-based AM technologies, direct energy deposition (DED) has emerged as a promising technique capable of producing high-volume parts within a reasonable printing time [8–10]. However, despite advancements such as multi-laser systems and powder reuse strategies, both LPBF and DED still face challenges associated with the long printing times required for large components. Additionally, assembling complex aerospace components (e.g., rocket nozzles) often requires welding operations. However, as widely documented in the literature [11,12], Ni-based alloys present welding challenges that are intrinsically linked to their microstructure. In particular, additively manufactured materials, which typically exhibit a coarse and highly oriented grain structure, tend to have different weldability characteristics compared to wrought materials, which generally feature fine and equiaxed grains. Therefore, investigating the weldability of additively manufactured Ni-based superalloys is crucial for expanding the applicability of laser-based AM in high-volume part fabrication.

Regarding the weldability of Ni-based alloys, potential issues include weld solidification cracking, heat-affected zone (HAZ) liquation cracking, strain-age cracking, and ductility dip cracking. Among these, Ni-based alloys are particularly susceptible to weld solidification cracking due to their austenitic solidification mode, which leads to strong interdendritic segregation and the precipitation of eutectic phases. While the weldability of wrought Ni-based alloys has been extensively studied [13–21], relatively few studies have focused on the weldability of AM Ni-based alloys. Notably, Raza et al. [22–24] investigated weld metal cracking in Alloy 718 fabricated by LPBF using weldability tests. Their research assessed liquation cracking susceptibility through longitudinal varestraint testing, examining welds performed both parallel and perpendicular to the build direction of the AM material. These tests revealed different cracking behaviors, attributed to the anisotropic microstructure typically observed in AM materials [25]. Moreover, studies have shown that the microstructure and chemistry of AM-produced materials can differ significantly from those of conventionally processed materials, potentially affecting weldability [26–28]. Recently, Guzman et al. [29] compared the weldability of LPBF 316 L with that of conventionally manufactured parts and found that nitrogen pickup during printing significantly influenced the material's weldability. Additionally, to the best of the authors' knowledge, the weldability of Ni-based superalloys fabricated by blown-powder laser-based DED has not yet been reported in the literature. This highlights the necessity of further research to understand the weldability of AM-fabricated Ni-based superalloys across different AM technologies.

This work focuses on Alloy 625 and Alloy 718 due to their importance in the aerospace industry. Alloy 625 is a solid-solution-strengthened alloy, primarily reinforced by molybdenum (Mo) and niobium (Nb), and is known for its good weldability among Ni-based superalloys. In contrast, Alloy 718 is a precipitation-strengthened alloy containing significant additions of titanium (Ti), aluminum (Al), and Nb, which promote the precipitation of a higher volume fraction of the γ'' phase (Ni_3Nb) compared to the γ' phase (Ni_3Al,Ti). This difference in phase volume fraction enhances resistance to strain-age cracking, making Alloy 718 one of the most widely used Ni-based alloys in the aerospace industry, particularly for the production of turbines and pressure vessels [11,12]. Since both alloys contain considerable Nb, the formation of detrimental phases (e.g., Laves phase) can compromise their weldability. Previous studies [30–33] have shown that silicon (Si), carbon (C), and especially Nb contribute to the formation of the Laves phase and NbC, which form at the end of solidification via eutectic reactions (γ/Laves and γ/NbC). These phases lower the liquidus and solidus temperatures, increasing the melting temperature range [32]. However, the effect of Nb is not entirely negative, as it can promote crack healing in practical applications due to the high eutectic content at the end of solidification. In fact, Alloy 625 has been shown to exhibit resistance to weld solidification cracking due to this crack-healing effect [11,14].

The present work evaluates the weld solidification cracking susceptibility of Alloy 625 and Alloy 718 produced by conventional mill-rolling, LPBF, and powder-blown laser-based DED. Susceptibility to weld solidification cracking is assessed using transverse varestraint testing [34], one of the most widely used methods for evaluating hot cracking defects due to its practicality. Additionally, Scheil-Gulliver solidification simulations and cracking indexes proposed by Kou [35,36] and Ramirez et al. [37,38] are employed for further analysis. Given the industrial significance of welding AM-fabricated sub-parts and the well-documented hot cracking susceptibility of wrought Ni-based superalloys, this study aims to provide a comprehensive assessment of the weld solidification cracking susceptibility of additively manufactured Alloy 625 and Alloy 718.

2. Experimental procedures

2.1. Material

Both nickel alloys, 625 and 718, were manufactured as plates using three different processes: conventional mill rolling, LPBF, and DED. Both AM processes utilize powder feedstock and a laser heat source to produce high-density printed plates. AM plates were tested after heat treatments designed to relieve residual stresses from the AM processes, dissolve segregation, and homogenize the microstructure [39,40]. For LPBF, the plates underwent stress relief, hot isostatic pressing, and solution heat treatment. For DED, the plates were subjected to stress relief and solution heat treatment. The bulk chemistry of the alloys, analyzed using Optical Emission Spectroscopy (OES, SPECTROMAXx), along with nitrogen and oxygen contents measured by Inert Gas Fusion Analysis (Leco TC600), is listed in Table 1.

2.2. Transverse varestraint testing

Susceptibility to solidification cracking was evaluated using transverse varestraint testing. This experiment was chosen due to its simplicity to assess weld solidification cracking. Fig. 1 shows the setup used for the transverse varestraint testing. The wrought and LPBF plates had dimensions of 152 mm × 51 mm × 5 mm, while the DED plates measured 156 mm × 62 mm × 5 mm. The three types of plates shared the same thickness. Prior to testing, the samples were cleaned with a stainless-steel wire wheel, followed by an ethanol rinse to remove any

Table 1
Chemical composition in wt% of Alloys 625 and Alloy 718. Nitrogen and Oxygen are listed in ppm.

Element	Alloy 625			Alloy 718		
	Wrought	DED	LPBF	Wrought	DED	LPBF
Ni	60.7	61.8	62.3	54.1	53.1	54.8
Cr	22.0	21.5	21.7	18.5	19.2	19.2
Fe	4.39	3.83	4.37	17.33	18.23	17.48
Mo	8.40	8.68	8.18	2.93	2.96	3.06
Co	0.09	0.02	0.06	0.28	0.03	0.04
W	0.03	0.01	0.03	0.02	0.01	0.03
Nb	3.32	3.43	2.76	4.89	4.88	3.67
Ti	0.20	0.16	0.07	1.01	0.90	0.82
Al	0.10	0.10	0.12	0.46	0.53	0.46
Si	0.16	0.13	0.17	0.10	0.06	0.13
Mn	0.43	0.16	0.07	0.12	0.04	0.04
C	0.063	0.027	0.054	0.037	0.046	0.080
N (ppm)	209.9	170.0	69.1	74.3	87.9	85.6
O (ppm)	6.6	50.8	206.8	4.8	33.8	176.1

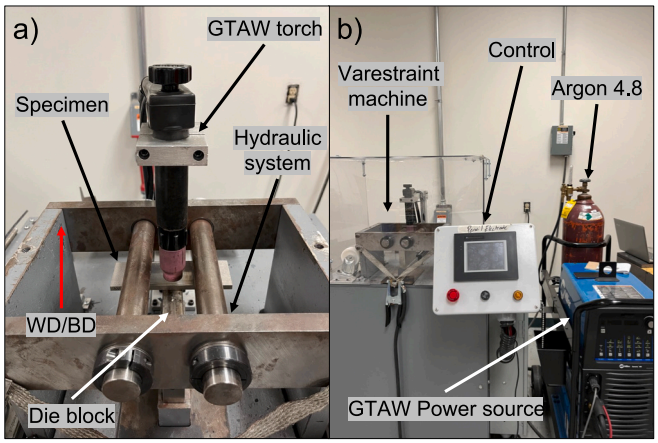

Fig. 1. Experimental setup of the transverse varestraint testing. a) Transverse varestraint testing machine and b) complete setup of the equipment.

contaminants.

Based on the recommendations of transverse varestraint experiments on nickel alloys in [41], mechanized Gas Tungsten Arc Welding (GTAW) parameters to obtain 10 mm-wide weld beads for the test were chosen and listed in Table 2. A 10 mm-wide weld pool ensures that cracking can be accurately observed and compared with other materials [29]. The weld beads were programmed to remain within the plates, measuring no more than 50 mm in length, with bending initiated 30 mm from the weld start at a rate of 250 mm/s. For each material, at least three repetitions were performed at strain levels of 0.5 %, 1 %, 2 %, 3 %, and 5 % using die blocks of radius of 635 mm, 159 mm, 106 mm, 80 mm, and 45 mm, respectively. The strains were chosen based on the saturated strain of nickel alloys to be between 2 % to 5 % [14]. The strain (ε) is given by eq. (1), recommended by the American Welding Society [42]:

$$\varepsilon = \frac{t}{2R + t} \tag{1}$$

where t is thickness of the specimen and R is the radius of the die blocks.

After testing, images of the surface of each plate were captured using a digital binocular microscope at 50× magnification. From the images, the total number of cracks (TNC), total crack length (TCL), maximum crack length (MCL), and maximum crack distance (MCD) were measured and reported with a 95 % interval of confidence. Measurements were done using Fiji ImageJ software [43]. Using the MCL and MCD results, it is possible to obtain the saturated strain, which is the strain at which the MCD does not increase anymore. Results were compared across materials and manufacturing processes.

2.3. Solidification simulations

Susceptibility to solidification cracking was evaluated using Scheil-Gulliver solidification simulations, the Crack Susceptibility Index (CSI) proposed by Kou [35,36], and the Flow Resistance Index (FRI) proposed by Ramirez et al. [37,38]. Scheil-Gulliver simulations were performed using Thermo-Calc 2024a with the Nickel-based Superalloys Database (TCNI12) and the chemical compositions listed in Table 1. These simulations provided the solidification temperature range (STR), which directly indicates the temperature range over which cracking occurs. The STR was determined based on the temperature gradient from 0 % to 95 % of the mole fraction of solid, with elements like C, N, and O considered as fast diffusers. The CSI proposed by Kou [35,36] was calculated based on the steepest slope of the temperature (T) versus the square root of the solid fraction $(fs)^{0.5}$ at fs = 98 %. The FRI proposed by Ramirez et al. [37,38] is a solidification cracking susceptibility index that accounts for the flow resistance of liquid metal within interdendritic channels. It estimates channel dimensions using Scheil-Gulliver curves and the STR, assuming a constant, arbitrary laminar flow rate near the end of the solidification interval (between 85 % and 98 % solid). The contributions of each segment of the channel length are integrated to determine the FRI, which is proportional to the material's cracking susceptibility. Dynamic viscosity is calculated using CALPHAD models, while the temperature profile is obtained through Thermo-Calc CALPHAD simulations. These simulation methods are designed for ease of use in industry and rely primarily on chemistry; as a result, they do not take microstructural features into account.

Table 2
GTAW parameters in the transverse varestraint testing.

Variable	Setting
Current	150 A
Travel speed	152 mm/min
Shielding gas	Argon 4.8
Flow rate	14.2 L/min
Electrode tip to work distance	2.4 mm
Weld start delay	5 s
Post-flow time	15 s
Deformation rate	250 mm/s
Electrode type	Tungsten with 2 % Lanthanum
Electrode diameter	2.4 mm

2.4. Electron microscopy characterization

Electron Backscatter Diffraction (EBSD) was performed using a Thermo Scientific Quattro Environmental Scanning Electron Microscope (ESEM) to analyze grain size and morphology at the weld bead centerline and the fusion line of the plates. Grain size was measured in the base metal and weld metal for both materials and each condition using the intercept method recommended by the ASTM E112–14 standard [44] and grain morphology was measured based on aspect ratio of the grains in the weld metal. This analysis aimed to investigate the microstructural evolution of the weld metal from the base material across the three different manufacturing processes. This is because the solidification simulation methods do not consider these features to assess weld solidification cracking. The data was processed using EDAX OIM Analysis software and MTEX toolbox. Samples were metallographically prepared by grinding with sandpaper up to 1200 grit, followed by polishing with fine diamond paste, and a final polishing step using colloidal silica to achieve a mirror-like surface.

3. Results and discussion

3.1. Transverse varestraint testing

The results of the transverse varestraint testing for alloys 625 and 718 are shown in Fig. 2 and Fig. 3, respectively. Both figures contain TNC, TCL, MCL, and MCD for each manufacturing condition with error bars representing a 95 % interval of confidence. Also, Fig. 4 shows the weld beads produced at 3 % strain during the experiment in the Alloy 625 for each condition, and Fig. 5 exposes with more detail the cracks of those beads at the region where the bending was applied. Fig. 6 and Fig. 7 show the same for the case of the Alloy 718. The images of both materials and each processing from where cracking measurements were taken can be found in the Supplementary Material of this work.

3.1.1. Transverse varestraint testing in alloy 625

In the case of Alloy 625, as shown in Fig. 2d, the LPBF condition was the most susceptible to weld solidification cracking, according to the MCD results. The wrought and DED conditions exhibited better and comparable resistance to weld solidification cracking. The LPBF condition reached a saturated strain at 3 %, with an MCD of approximately 2.35 ± 0.16 mm, whereas the wrought and DED conditions reached a saturated strain at 2 %, with MCD values of 1.56 ± 0.06 mm and 1.72 ±

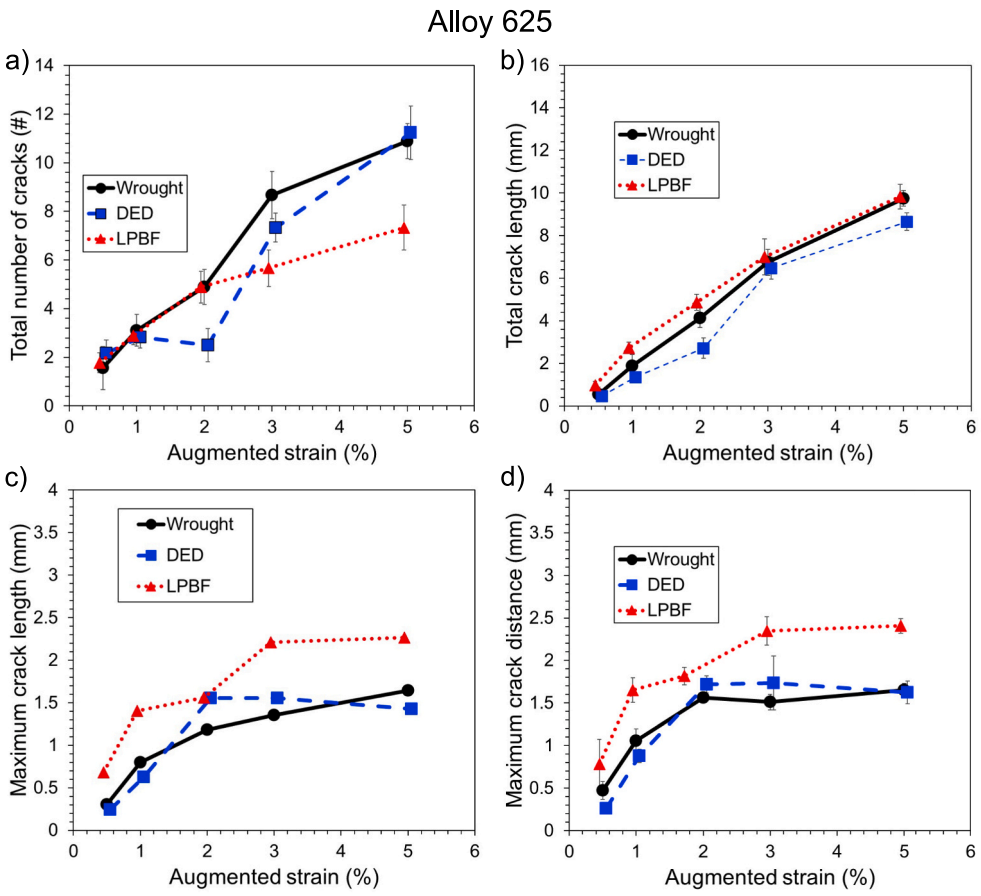

Fig. 2. Alloy 625 transverse varestraint testing results. a) TNC, b) TCL, c) MCL, and d) MCD. Results reported with a 95 % interval of confidence.

0.10 mm, respectively. The LPBF error bars never overlapped with the other processes and the values of MCD were bigger resulting in higher cracking susceptibility. On the other hand, the error bars of the wrought and the DED conditions overlapped resulting in the same values of MCD. The results of the wrought Alloy 625 are in accordance with that obtained by Lippold et al. [14], which indicated the same saturated strain at 2 % and similar values of MCD for the same material.

The MCL results followed a similar trend to the MCD results. However, the TNC results after reaching the saturated strain were surprisingly lower for the LPBF condition. In contrast, the TCL results for all three conditions were similar after passing the saturated strain. For instance, at 5 % strain, the TNC for the LPBF condition was 7, while for the other conditions, it exceeded 10. This suggests that although fewer cracks were observed in the LPBF condition, these cracks were larger. This observation is confirmed in Fig. 4 and Fig. 5, which clearly shows the larger size of the cracks in the LPBF condition at 3 % of strain compared to the other conditions. Based on transverse varestraint testing, the susceptibility of Alloy 625 to weld solidification cracking can be ranked from most to least resistant as follows: wrought, DED, and LPBF conditions.

3.1.2. *Transverse varestraint testing in alloy 718*

In the case of Alloy 718, as shown in Fig. 3d of the MCD results, both AM processes exhibited higher susceptibility to weld solidification cracking compared to the wrought condition. For the DED condition, the saturated strain was easily localized at 2 % strain, with an MCD of 2.93 ± 0.41 mm. In the wrought condition, the saturated strain was similarly distinct, occurring at approximately 1 % strain, with an MCD of 2.01 ± 0.12 mm. However, in the LPBF condition, the saturated strain was not clearly defined, as the MCD continued increasing, reaching 3.01 ± 0.33 mm at 5 % strain. These results indicate that the saturated strain is lowest in the wrought condition and progressively higher in the DED and LPBF conditions, with larger cracks observed in the AM processes.

The MCL results followed a trend similar to the MCD results. Additionally, the TNC values were comparable across all three conditions; however, the TCL was larger in the AM processes. For instance, at 5 % strain, the TNC was approximately 8 for all conditions, while the TCL was around 13 mm in the AM processes, compared to 10.68 ± 0.52 mm in the wrought condition. This means that cracks were bigger in the AM processes. The crack dimensions at 3 % strain, illustrated in Fig. 6 and Fig. 7, show very similar crack sizes for the wrought and LPBF conditions, with slightly larger cracks in the DED condition. Based on transverse varestraint testing, the susceptibility of Alloy 718 to weld solidification cracking can be ranked from most to least resistant as follows: wrought, LPBF, and DED conditions.

The majority of the literature on wrought Alloy 718 employs longitudinal varestraint testing to assess HAZ liquation cracking [16,18,21,45,46]. More recent studies on LPBF Alloy 718 by Raza et al. [22–24] also investigated liquation cracking susceptibility using longitudinal varestraint testing. In their research, higher susceptibility was attributed to the significantly larger grain size of the LPBF product [22]. Additionally, smaller cracks were observed in samples subjected to solution heat treatment, due to the reduction of eutectic products [23]. They also studied the effect of building direction on longitudinal varestraint testing, finding cracking differences in the HAZ, but no significant differences in the fusion zone [24]. No literature was found reporting results from transverse varestraint testing on this material.

When comparing the results for Alloys 625 and 718, it can be concluded that, in transverse varestraint testing, Alloy 625 exhibits greater resistance to weld solidification cracking than Alloy 718. These results align with previous studies comparing these alloys [13].

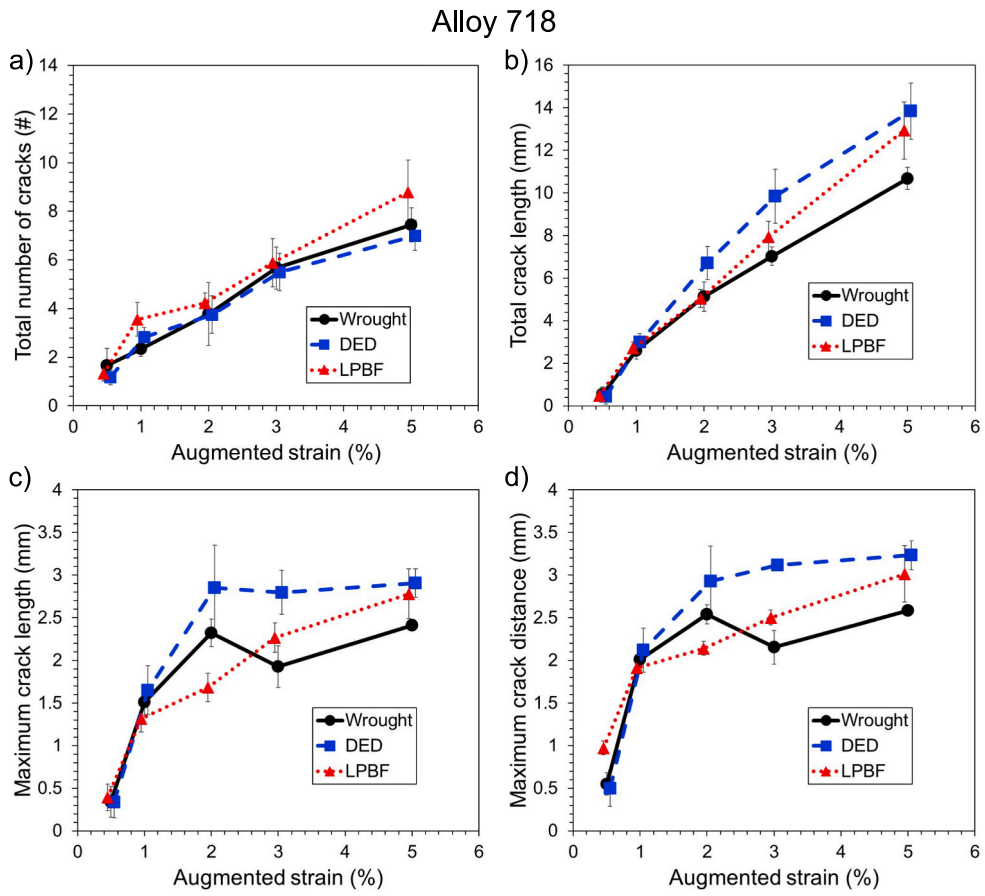

Fig. 3. Alloy 718 transverse varestraint testing results. a) TNC, b) TCL, c) MCL, and d) MCD. Results reported with a 95 % interval of confidence.

3.2. Solidification simulations

The response to weld solidification cracking in the transverse varestraint testing depends on multiple factors. When comparing similar alloys, variations primarily arise from differences in chemistry and the microstructural evolution influenced by the manufacturing process. Nickel alloys are particularly susceptible to weld solidification cracking due to their austenitic microstructure and the partitioning of alloying elements especially Nb into the liquid phase during solidification. This partitioning promotes the formation of low-melting eutectic products, expanding the solidification temperature range and reducing resistance to cracking [11]. Additionally, the austenitic primary solidification microstructure is characterized by solidification sub-grain boundaries enriched in segregated elements and large, straight solidification grain boundaries—both of which facilitate crack propagation during solidification [47,48].

Scheil-Gulliver curves, as well as the CSI and the FRI, are chemistry-based methods. Since they do not account for microstructural and mechanical features, they have certain limitations. However, these methods are widely used and have demonstrated good correlation with experimental results, making them valuable as complementary tools for assessing weldability. Although the CSI was initially developed for aluminum alloys [35,36], it has shown good correlation with other materials, including nickel alloys. Xia and Kou [19] applied the CSI to study a new weldability test for nickel alloys, the transverse-motion test. Their findings demonstrated a strong correlation between the CSI, cast pin test, and transverse-motion test results. More recently, Ariaseta et al. [21] used STR values derived from Scheil-Gulliver curves, along with the CSI, to evaluate the susceptibility to weld cracking in G27 and Alloy 718. Their results aligned well with susceptibility trends observed in longitudinal varestraint testing.

3.2.1. Solidification simulations for alloy 625

Scheil-Gulliver simulations were conducted using the chemical compositions in Table 1 for each condition. The Scheil-Gulliver curves are depicted in Figs. 8 and Fig. 9 for the Alloy 625 and the Alloy 718, respectively. Both alloys solidify as FCC, and MC and the Laves phase at the end of solidification form for all conditions. The Laves phase impact resistance to weld solidification cracking [30–33]. The solidification path of the Scheil-Gulliver curves resemble a columnar dendritic grain structure near the grain boundary, providing insights into the ease of liquid feeding into cracks [35]. The steeper change in solidification fraction was observed in the LPBF condition suggesting easier formation of narrow liquid films, which can aid in crack propagation. Also, from the curves, the STR was calculated and is shown in Fig. 10 for all conditions of the Alloy 625 up to 95 % mole fraction of solid. The ranges were 181 °C for the wrought, 203 °C for the DED, and 148 °C for the LPBF. These STR values are lower than those reported for Alloy 625 by Lippold et al. (243 °C) [14].

Interestingly, Scheil-Gulliver solidification paths indicated that the LPBF is more prone to narrow liquid films. However, the LPBF condition had the lowest STR indicating better resistance to weld solidification cracking. This contradicts the transverse varestraint testing results of MCD in Fig. 2d. This discrepancy may be related to the chemistry of the LPBF Alloy 625, shown in Table 1, which does not align with the nominal composition of the Alloy 625 [49]. Specifically, the Nb content in the LPBF condition is 2.76 wt%, which is below the specification range of 3.15–4.15 wt% for this alloy. Nb influences the solidification sequence and, consequently, the solidification range, where a higher Nb content increases the solidification range [11,33]. Low Nb content tends to reduce the matrix/Laves eutectic content since the majority of Nb present in the liquid is consumed by the first eutectic reaction (liquid → matrix + (Nb, Ti)C), following the solidification path of Nb-bearing Ni-

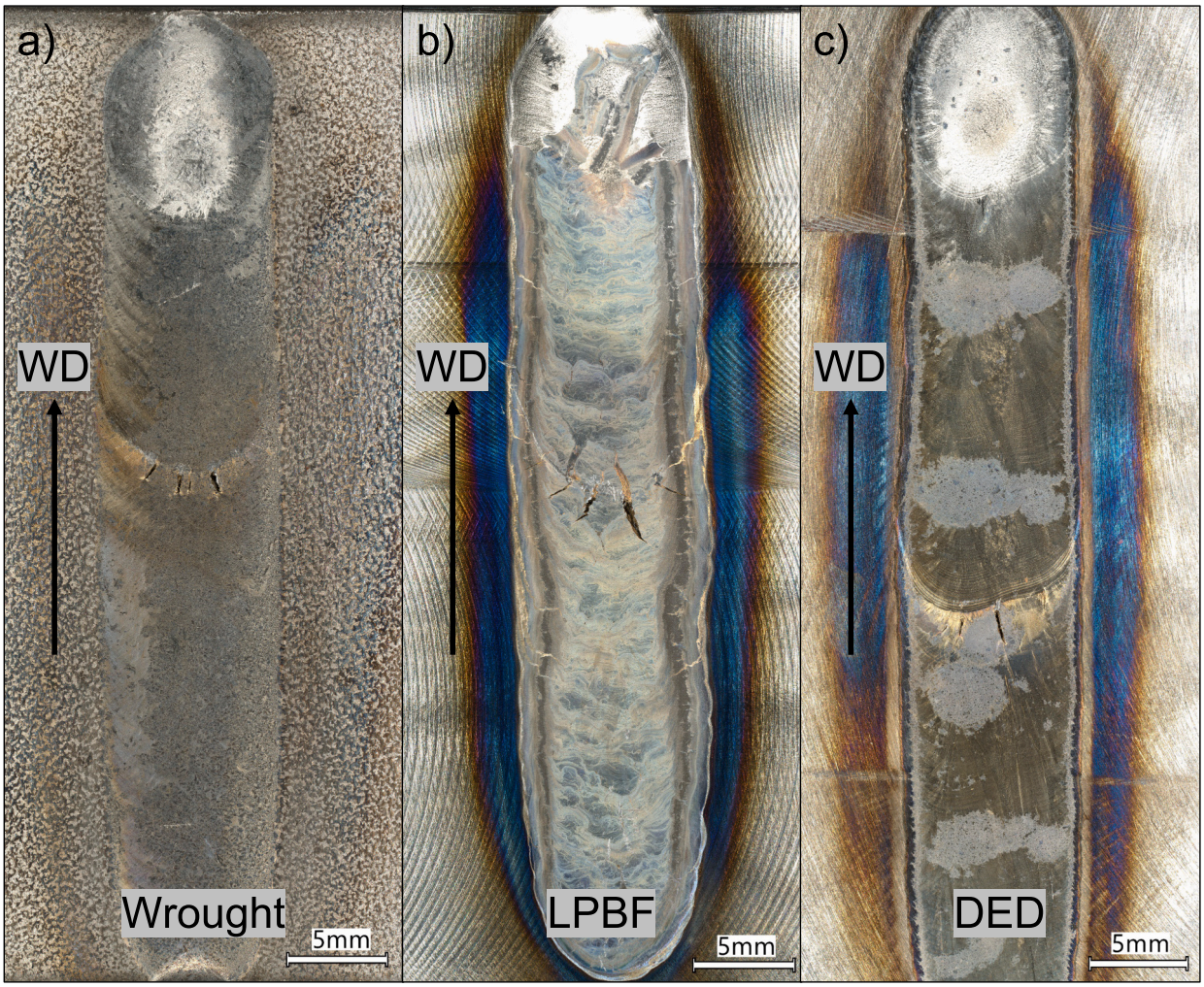

Fig. 4. Alloy 625 weld beads produce at 3 % strain. a) Wrought, b) LPBF, and c) DED.

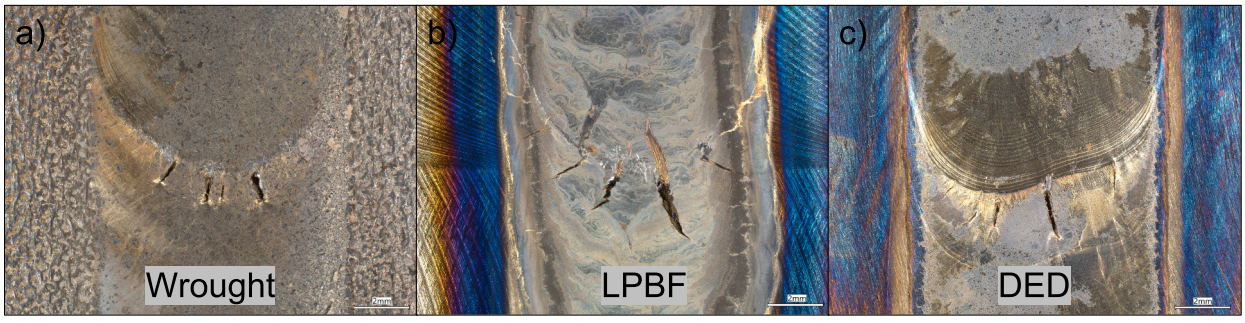

Fig. 5. Alloy 625 cracking at 3 % strain. a) Wrought, b) LPBF, and c) DED.

based superalloys proposed by DuPont et al. [31,32]. Therefore, as Nb content is lower in the LPBF Alloy 625, it is expected a lower STR.

3.2.2. *Solidification simulations for alloy 718*

Scheil-Gulliver simulations of Alloy 718, shown in Fig. 9, reveal the presence of the Laves phase at the end of solidification across all three conditions, which can negatively impact resistance to weld solidification cracking. Furthermore, the solidification paths for the wrought and DED conditions are similar and less steep than that of the LPBF condition. The composition of LPBF Alloy 718, as shown in Table 1, deviates from the nominal composition of Alloy 718 [49], particularly in its Nb content, which is 3.67 wt%—below the specification range of 4.75–5.50 wt%.

Alloy 718 is a precipitation-strengthened nickel alloy that forms the γ'' phase (Ni_3Nb). The Nb content is crucial as it promotes γ'' formation, delaying the γ' phase (Ni_3Al,Ti) and thereby reducing strain-age cracking [12]. The Scheil-Gulliver curves suggest that the lower Nb content in the LPBF condition promotes sharper dendrites and narrower liquid films compared to the other conditions. However, the solidification temperature ranges up to 95 % mole fraction of solid, as shown in Fig. 10, are similar among the analyzed conditions: 205 °C (wrought), 195 °C (DED), and 204 °C (LPBF). Based on the STR obtained from Scheil-Gulliver simulations, it is not possible to determine which

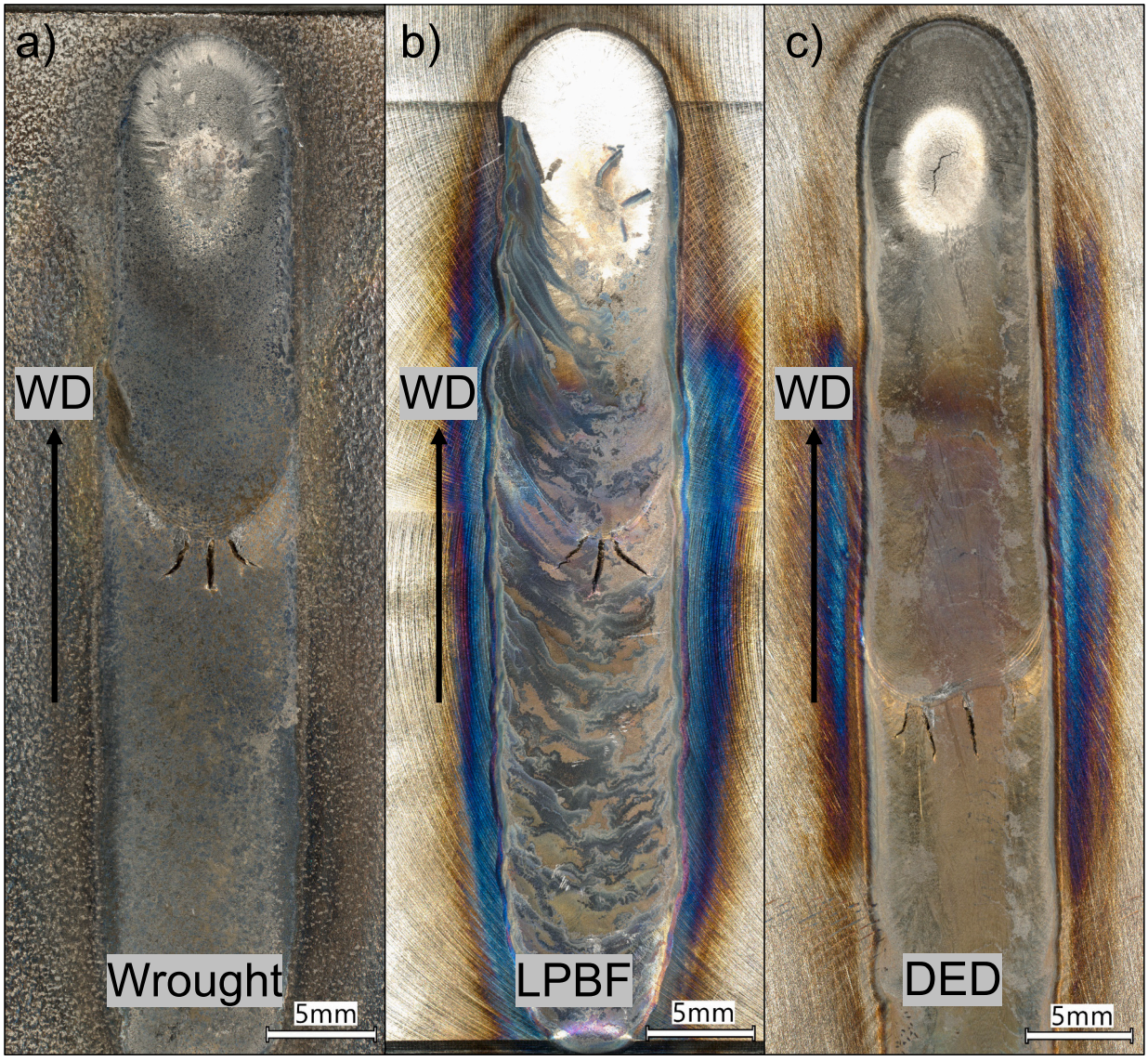

Fig. 6. Alloy 718 weld beads produce at 3 % strain. a) Wrought, b) LPBF, and c) DED.

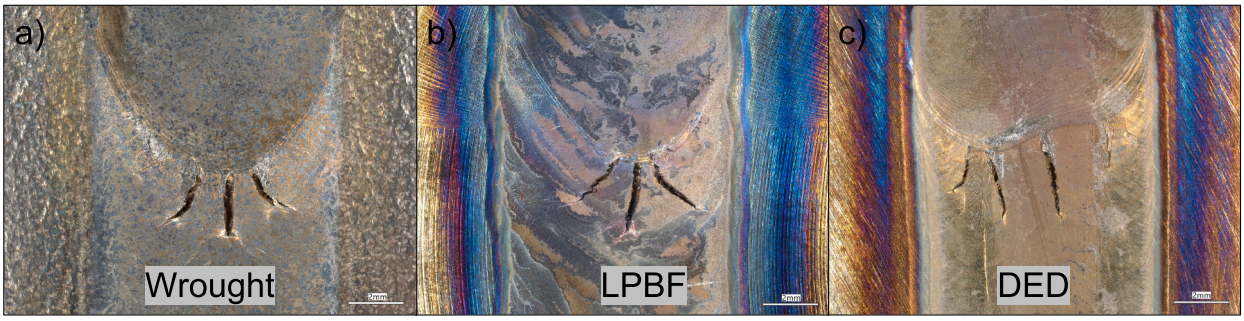

Fig. 7. Alloy 718 cracking at 3 % strain. a) Wrought, b) LPBF, and c) DED.

condition is more or less susceptible to solidification cracking, but it is possible to see that the STR was higher for the Alloy 718 than the Alloy 625. This matches with the susceptibility to hot crack obtained from the experimental results of the transverse varestraint test and literature [13]. These STR values are lower than those reported for Alloy 718 by Ariaseta et al. (283 °C) [21].

3.2.3. *Solidification simulations, CSI and FRI*

Using data from the Scheil-Gulliver simulations, the CSI and FRI indices were obtained. Fig. 11 presents the temperature versus the square root of the fraction solid (fs) curves for each material, along with the CSI result for fs = 0.98 and the FRI values. According to the CSI, the most susceptible condition to solidification cracking is DED for Alloy 625 and LPBF for Alloy 718. The least susceptible condition is LPBF for

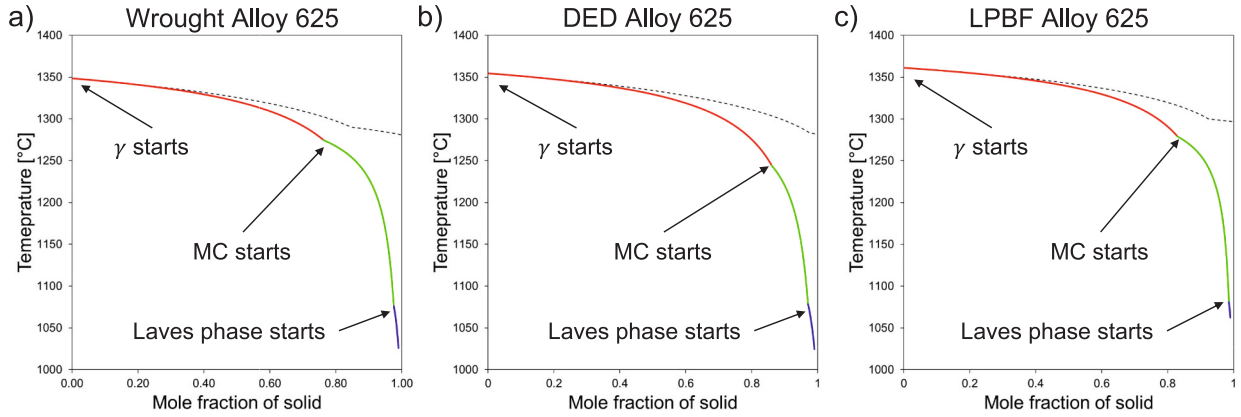

Fig. 8. Alloy 625 Scheil-Gulliver Simulations. a) Wrought Alloy 625, b) DED Alloy 625, and c) LPBF Alloy 625.

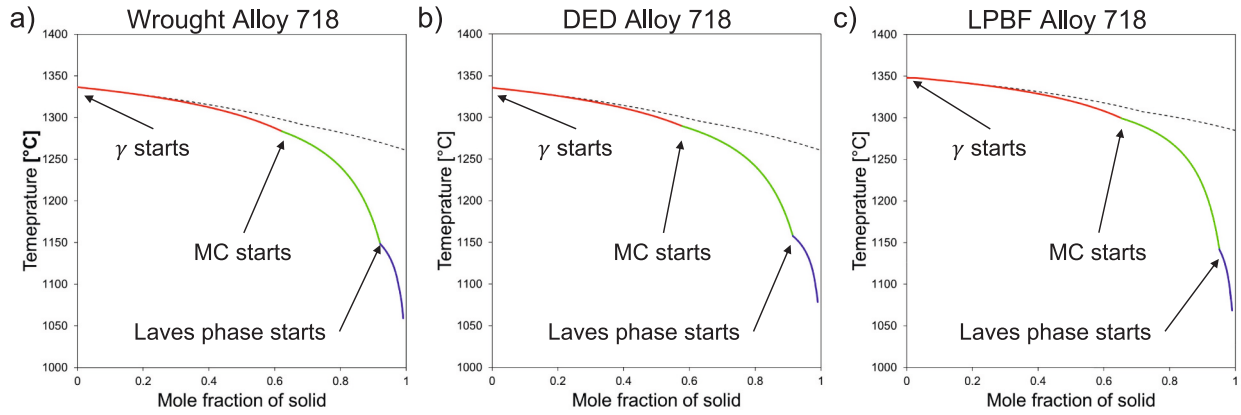

Fig. 9. Alloy 718 Scheil-Gulliver Simulations. a) Wrought Alloy 718, b) DED Alloy 718, and c) LPBF Alloy 718.

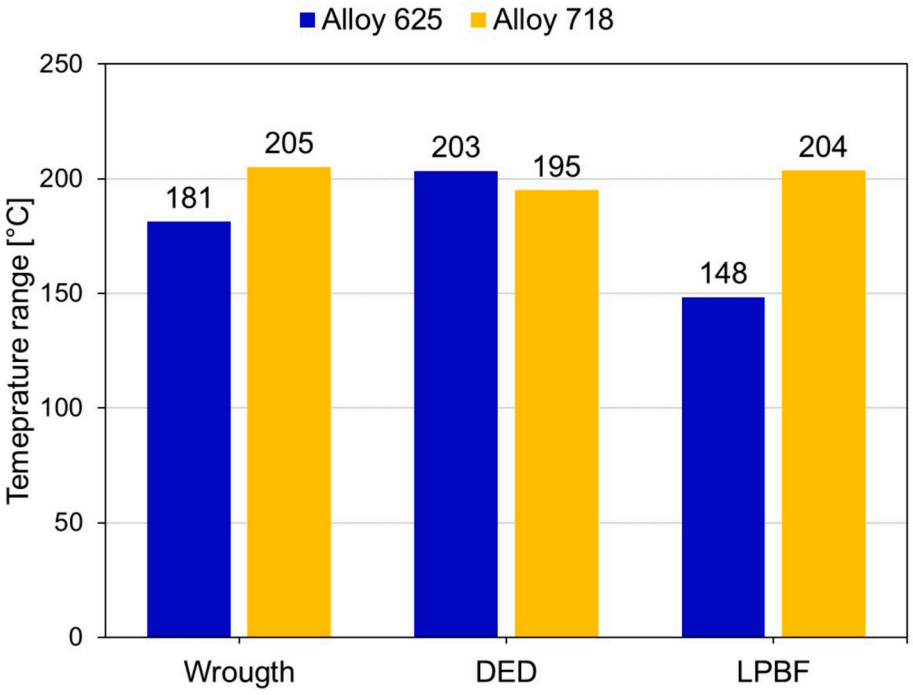

Fig. 10. Solidification temperature range up to 95 % mole fraction of solid taken from the Scheil-Gulliver curves. Alloy 625 in blue and Alloy 718 in orange. (For interpretation of the references to colour in this figure legend, the reader is referred to the web version of this article.)

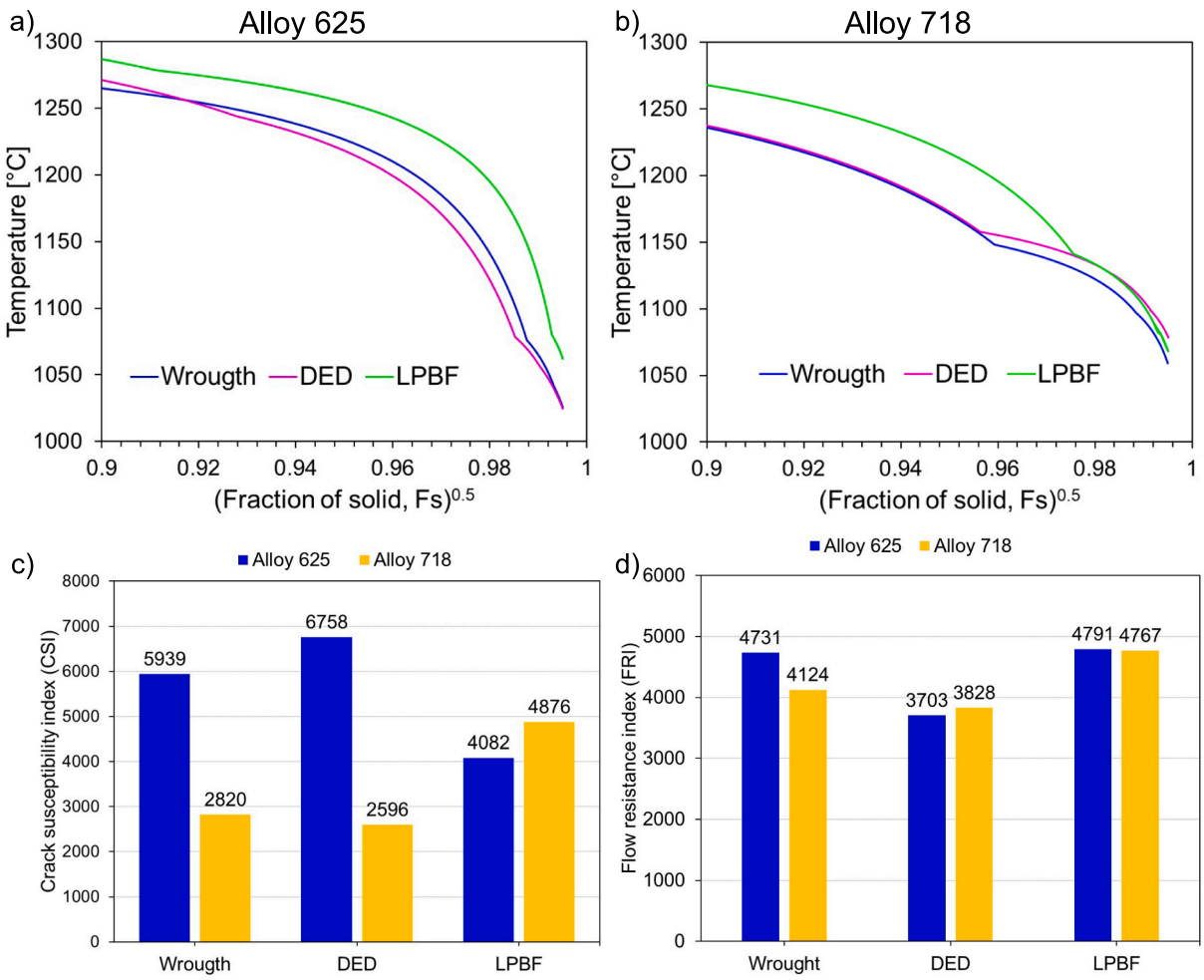

Fig. 11. Solidification simulations. a) T vs. $(fs)^{0.5}$ curve of Alloy 625, b) T vs. $(fs)^{1/2}$ curve of Alloy 718, c) CSI corresponding with the steepest slopes at $(fs)^{0.5} = 0.98$, and d) the FRI. Alloy 625 in blue and Alloy 718 in orange in c) and d). (For interpretation of the references to colour in this figure legend, the reader is referred to the web version of this article.)

Alloy 625, while for Alloy 718, it is DED and wrought.

For Alloy 625, the CSI correlates well with the STR but not with transverse varestraint testing. In contrast, for Alloy 718, the CSI does not correlate with either the STR or the transverse varestraint testing. According to the FRI, the most susceptible conditions are wrought and LPBF for Alloy 625, and LPBF for Alloy 718. The FRI results for Alloy 625 align with transverse varestraint testing but not with the STR, while the results for Alloy 718 do not match either transverse varestraint testing or STR.

Notably, both indices indicate higher susceptibility values for Alloy 625 compared to Alloy 718. However, transverse varestraint testing has shown that Alloy 625 is more resistant to solidification cracking than Alloy 718 [13]. These findings suggest that the models need improvement to better align with transverse varestraint testing and other materials, as some were originally developed for aluminum alloys [35]. Although the models have shown some correlation with experimental weldability testing [19,36], they only account for chemical composition and do not consider microstructural and mechanical factors, which can also influence cracking susceptibility.

3.3. Effect of oxygen on cracking

The LPBF Alloy 625 exhibited an oxygen content of 206.8 ppm, while the LPBF Alloy 718 had an oxygen content of 176.1 ppm. Compared to the other conditions reported in Table 1, these values were higher. This oxygen uptake originates from the LPBF printing process and can come from the shielding gas, printing atmosphere, or the powder itself [27]. While the role of oxygen in weld solidification cracking is not fully understood, studies on austenitic stainless steels and iron [26,50–54] suggest that oxygen can influence melt pool geometry by altering flow direction during welding. This phenomenon, known as the Marangoni effect, occurs due to variations in surface tension along the melt pool interface. Typically, liquid metal flows outward from regions of lower surface tension (hotter areas) to regions of higher surface tension (cooler areas). However, surface-active elements such as O, S, Se, and Te can increase surface tension at the center of the melt pool, reversing the flow direction inward [54]. This inward flow helps distribute heat and molten material within the weld pool. In iron-oxygen alloys, the gradient of surface tension with temperature reverses at approximately 100 ppm oxygen [50,52–54]. In a recent study, Yang et al. [55] used synchrotron X-ray imaging to monitor the Marangoni effect in the keyhole formation of LPBF 316 L stainless steel. They concluded that inward fluid flow is a common phenomenon in LPBF. This change in flow can alter segregation patterns within the melt pool, potentially affecting weld solidification cracking. Further research is needed to investigate the specific effects of oxygen on weld solidification cracking, as no studies have focused explicitly on this topic.

3.4. Electron microscopy characterization

3.4.1. Characterization of alloy 625

Samples subjected to a 2 % strain were selected for EBSD analysis.

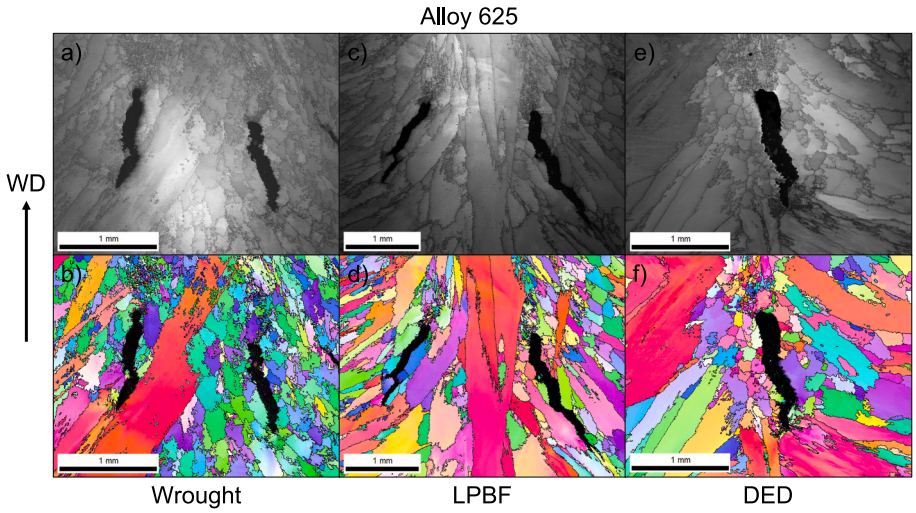

Fig. 12. Alloy 625, cracking at 2 % strain. a) and b) Wrought Alloy 625, c) and d) LPBF Alloy 625, and e) and f) DED Alloy 625.

Fig. 12 shows the orientation maps of Alloy 625 for the three processing conditions at 2 % strain in the bending region of the transverse varestraint test. The EBSD analysis was performed along the weld centerline, where cracking occurred. From the images, it is evident that both AM conditions exhibited cracks of similar sizes. According to the values in Fig. 2d, the MCD for the wrought, LPBF, and DED conditions were 1.56 ± 0.06 mm, 1.82 ± 0.10 mm, and 1.72 ± 0.10 mm, respectively. This slight variation in crack size can be attributed to differences in grain morphology and size.

The wrought Alloy 625 contains more tortuous grains and fewer columnar grains compared to both AM conditions. Conversely, both the LPBF and DED conditions are characterized by predominantly long and straight columnar grains. Additionally, the LPBF Alloy 625 exhibited axial grains at the weld centerline, which act as stress concentrators during welding. In contrast, while the DED Alloy 625 also contains columnar grains, smaller grains were nucleated at the weld centerline. The presence of axial grains at the centerline of the LPBF Alloy 625 likely explains its greater susceptibility to solidification cracking observed in the transverse varestraint test.

EBSD analysis was also conducted at the trailing edge of the weld pool in each Alloy 625 condition to examine grain evolution from the base material through the HAZ and into the fusion weld. As shown in Fig. 13, the wrought Alloy 625 exhibits smaller grains compared to both AM conditions. The LPBF and DED conditions have larger grains, particularly in the HAZ, which serve as substrates for the growth of even larger grains in the fusion zone.

The grain size of the base metal and weld metal, along with the aspect ratio in the weld metal, were measured and reported in Fig. 14. Because the intercept method does not account for grain morphology, the aspect ratio was also measured. The data show that the grain size in the base metal was larger for both AM processes compared to the wrought Alloy 625: 9.99 ± 0.23 μm for the wrought, 38.84 ± 4.47 μm for the DED, and 23.16 ± 1.76 μm for the LPBF. In the weld metal, the grain size of the DED Alloy 625 was larger than that of the wrought and LPBF conditions, which exhibited similar grain sizes: 31.34 ± 4.13 μm for the wrought, 50.05 ± 11.85 μm for the DED, and 28.79 ± 3.20 μm for the LPBF.

According to the aspect ratio results, all three processes produced elongated grains with aspect ratios greater than 1, with the LPBF material exhibiting the highest values. These results indicate that changes in grain size and morphology occur in all three materials. The influence of grain size and morphology affect solidification cracking. Previous studies on nickel alloys have reported that increased grain size negatively impacts resistance to solidification cracking [22,56,57]. For example, larger grains tend to reduce the availability of boundaries to accommodate strain during thermal contraction, lead to more pronounced elemental segregation at grain boundaries, and facilitate crack propagation [58]. Although, grain size of the weld metal resulted to be similar for the wrought and LPBF, combine results with aspect ratio indicated that big parent grains in the base metal result in big and

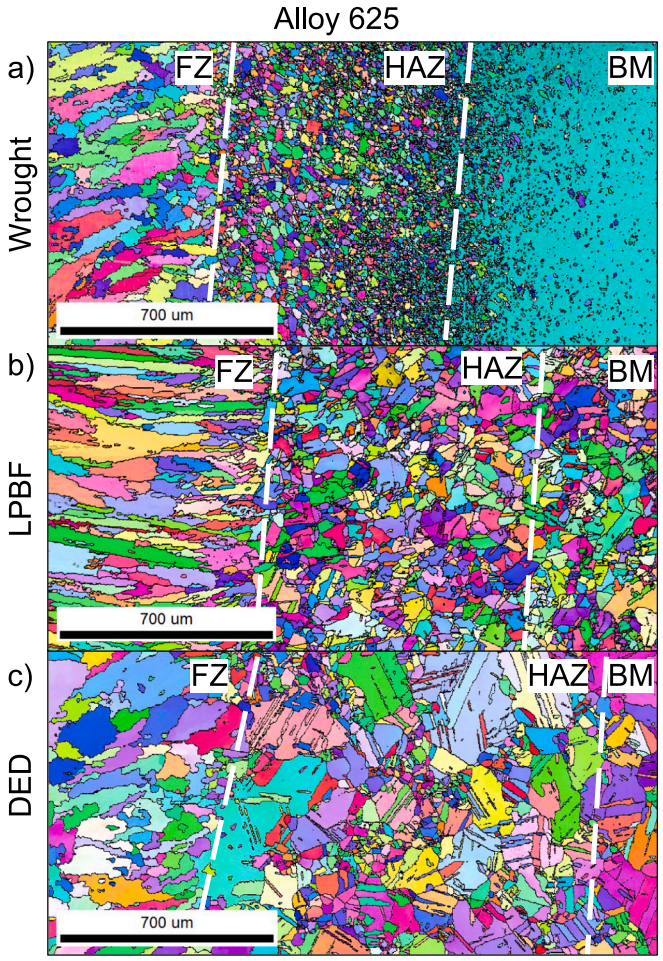

Fig. 13. Alloy 625, trailing edge of the weld pool. a) Wrought Alloy 625, b) LPBF Alloy 625, and c) DED Alloy 625.

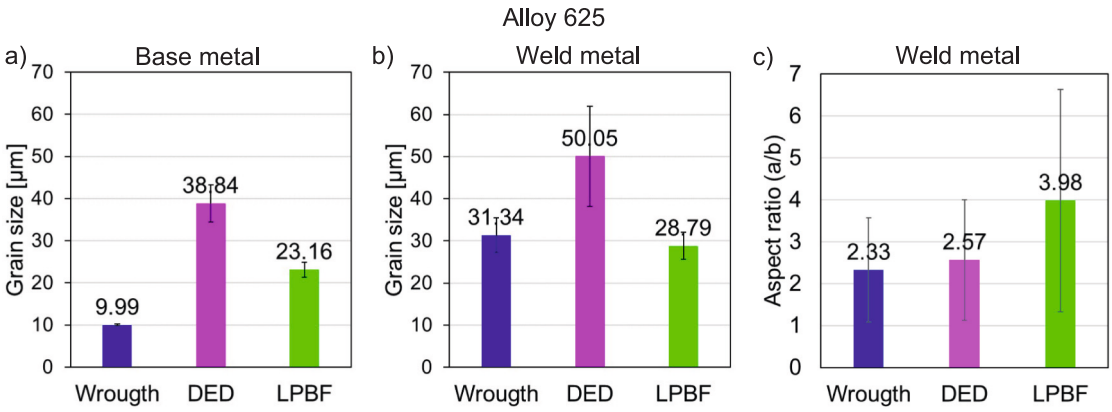

Fig. 14. Alloy 625. Grain size of the a) base metal and b) weld metal, and c) grain aspect ratio of the weld metal.

columnar grains in the weld metal. This confirms that the present of big grains in the base metal in the LPBF Alloy 625 affected the response to hot cracking in the transverse varestraint.

3.4.2. *Characterization of alloy 718*

The orientation maps of Alloy 718 processed under the three different conditions at 2 % strain in the bending region of the transverse varestraint test are presented in Fig. 15. The images reveal that cracks in the DED Alloy 625 were significantly larger than those in the wrought and LPBF conditions. According to the MCD results from Fig. 3d, the transverse varestraint testing showed that the wrought Alloy 718 had an MCD of 2.54 ± 0.11 mm, while the LPBF Alloy 718 measured 2.14 ± 0.08 mm, and the DED Alloy 718 exhibited the highest value at 2.93 ± 0.41 mm. The increased MCD in the DED condition was attributed to the presence of larger columnar grains at the weld centerline compared to the other conditions. Unlike LPBF Alloy 625, axial grains at the weld centerline were not observed in any Alloy 718 condition.

The EBSD analysis at the trailing edge of the weld pool in Alloy 718 (Fig. 16) indicates that substrate grains in the HAZ of both AM conditions were larger than those in the wrought Alloy 718. These larger grains in the HAZ facilitated the nucleation of even larger columnar grains in the fusion zone, which may have influenced the material's susceptibility to weld solidification cracking during the transverse varestraint test.

The grain size and morphology results in Fig. 17 showed that while there was a clear difference in base metal grain size between the wrought and AM materials, the weld metal grain size was relatively similar across all three processes. In the base metal, the grain size was 13.55 ± 0.50 μm for the wrought Alloy 718, 37.67 ± 4.97 μm for the LPBF Alloy 718, and 33.56 ± 2.44 μm for the DED Alloy 718. In the weld metal, the grain size measured 31.93 ± 2.70 μm for the wrought Alloy

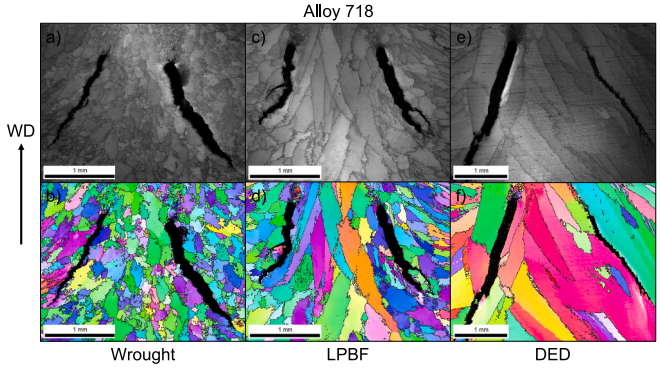

Fig. 15. Alloy 718, cracking at 2 % strain. a) and b) Wrought Alloy 718, c) and d) LPBF Alloy 718, and e) and f) DED Alloy 718.

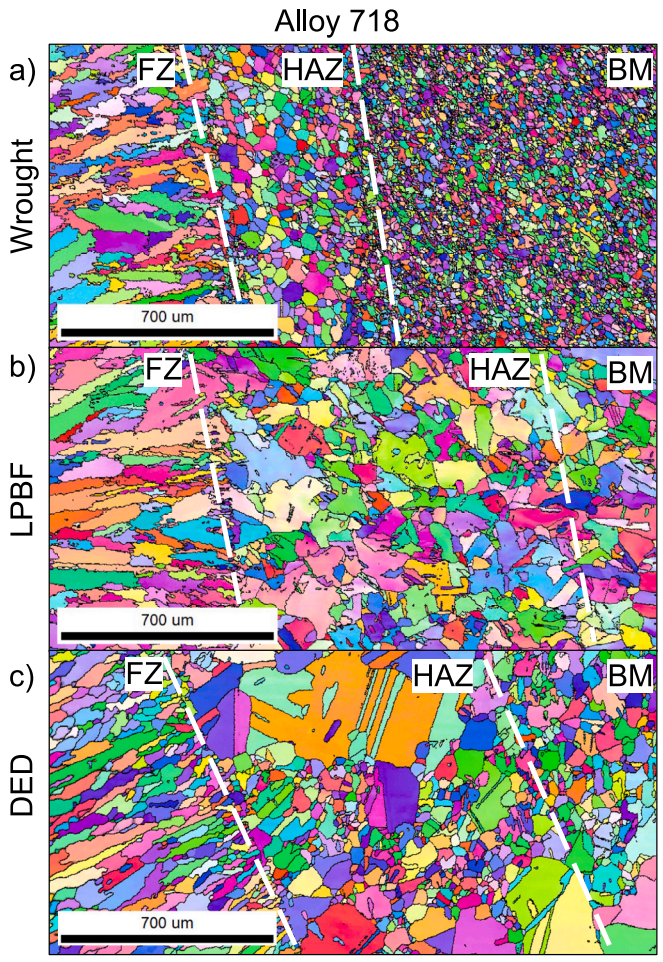

Fig. 16. Alloy 718, trailing edge of the weld pool. a) Wrought Alloy 718, b) LPBF Alloy 718, and c) DED Alloy 718.

718, 34.11 ± 1.52 μm for the LPBF Alloy 718, and 37.35 ± 5.39 μm for the DED Alloy 718. The aspect ratio results were similar for all three processes, as indicated by overlapping error bars, and predominantly exhibited an elongated grain structure. Large grain size and columnar morphology contribute to localized reductions in yield strength [59–61]. A lower yield strength during solidification may increase the risk of solidification cracking. These results confirm that the main difference playing a role in the susceptibility of the material in the transverse varestraint is the grain size of the base material.

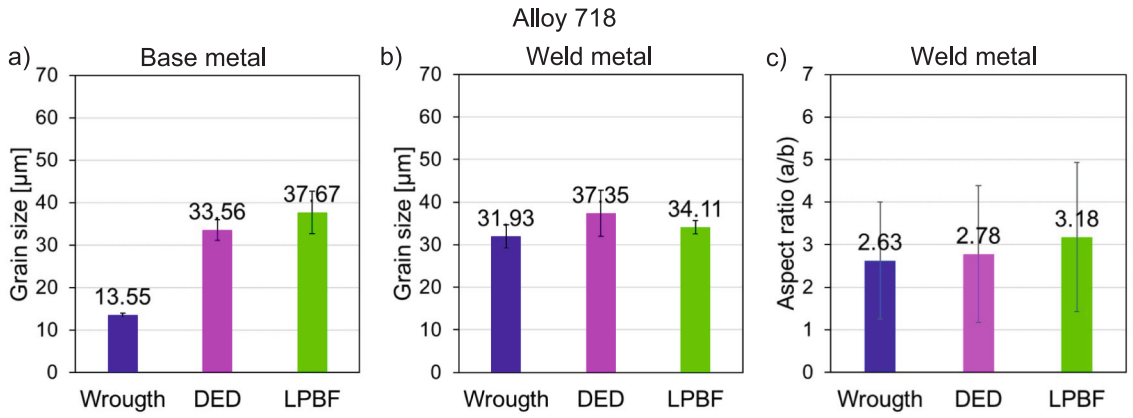

Fig. 17. Alloy 718. Grain size of the a) base metal and b) weld metal, and c) grain aspect ratio of the weld metal.

4. Conclusions

This study assessed the weld solidification cracking susceptibility of Alloys 625 and 718 produced by wrought (mill-rolled), LPBF, and DED using transverse varestraint testing, Scheil-Gulliver simulations (STR), and the CSI and FRI indexes. The key findings are summarized as follows:

- In Alloy 625, the LPBF condition exhibited the highest MCD in transverse varestraint testing. The LPBF condition reached saturated strain at 3 % with an MCD of 2.35 ± 0.16 mm, whereas the wrought and DED conditions reached saturation at 2 % strain, with MCD values of 1.56 ± 0.06 mm and 1.72 ± 0.10 mm, respectively. The higher susceptibility of LPBF Alloy 625 was attributed to the presence of axial columnar grains in the weld centerline.
- In Alloy 718, the DED condition showed the highest MCD in transverse varestraint testing, reaching saturated strain at 2 % with an MCD of 2.93 ± 0.41 mm. The wrought condition reached saturation at 1 % strain with an MCD of 2.01 ± 0.12 mm, while the LPBF condition did not exhibit a clear saturation strain, with its MCD increasing to 3.01 ± 0.33 mm at 5 % strain. The greater susceptibility of AM Alloy 718 was attributed to the large and elongated grains in the fusion zone.
- Wrought materials demonstrated greater resistance to weld solidification cracking, as indicated by their lower MCD values in transverse varestraint testing.
- The combined EBSD and varestraint testing results showed that grain size and morphology are the primary differences among the three materials. Larger substrate grains in AM materials led to the formation of large and elongated grains in the fusion zone, affecting the weld solidification cracking response. The base material's grain size plays a key role in determining weld metal grain morphology and cracking susceptibility.
- The CSI and FRI cracking susceptibility indexes did not correlate with the experimental transverse varestraint test results, as these models rely solely on chemistry and do not account for microstructural and mechanical factors.
- Scheil-Gulliver simulations revealed similar solidification path morphologies and comparable solidification temperature ranges across all processing conditions. While STR results did not match the experimental cracking susceptibility, they aligned with the chemical composition of the alloys, particularly regarding Nb content and the known higher cracking susceptibility of Alloy 718 compared to Alloy 625.

Oxygen pickup, especially in LPBF processing, remains a significant concern and should be addressed. Further varestraint and microscopy experiments on different alloy systems are recommended to confirm these findings, particularly regarding the impact of oxygen content in LPBF-produced parts on cracking susceptibility.

CRediT authorship contribution statement

Jhoan Guzman: Writing – review & editing, Methodology, Investigation, Formal analysis, Conceptualization. **Kaue C. Riffel:** Writing – review & editing, Investigation, Formal analysis. **William Evans:** Writing – original draft, Investigation, Data curation. **Eric Brizes:** Writing – review & editing, Formal analysis, Data curation. **Nicholas Avedissian:** Writing – review & editing, Investigation. **Francisco Werley Cipriano Farias:** Writing – review & editing, Formal analysis, Data curation. **Antonio J. Ramirez:** Visualization, Validation, Supervision, Project administration, Funding acquisition.

Funding

Funding for testing and materials was provided by the Liquid Engines Project Office of NASA Marshall Spaceflight Center. Partial financial support was received from the Welding Engineering Program of The Ohio State University.

Declaration of competing interest

The authors declare that they have no known competing financial interests or personal relationships that could have appeared to influence the work reported in this paper.

Acknowledgments

The authors thank the Welding Engineering Program of The Ohio State University. Thanks are given to the propulsion laboratory and the liquid engines project office at NASA Marshall Spaceflight Center for their insight and support. Thanks to the Center for Electron Microscopy and Analysis (CEMAS), the place where SEM images were taken. Jhoan Guzman expresses his appreciation to the Fulbright Colombian Program (cohort 2021), the Ministry of Science, Technology, and Innovation of Colombia, and the Manufacturing and Materials Joining Innovation Center (Ma2JIC) for funding his PhD. Francisco Werley Cipriano Farias acknowledges Fundação para a Ciência e a Tecnologia (FCT-MCTES) for funding his PhD Grant 2022.13870.BD.

Appendix A. Supplementary data

Supplementary data to this article can be found online at https://doi.org/10.1016/j.jmapro.2025.02.051.

References

[1] Balaguru S, Gupta M. Hardfacing studies of Ni alloys: a critical review. J Mater Res Technol 2021;10:1210–42. https://doi.org/10.1016/j.jmrt.2020.12.026.

[2] Mahesh K, Philip JT, Joshi SN, Kuriachen B. Machinability of Inconel 718: a critical review on the impact of cutting temperatures. Mater Manuf Process 2021;36:753–91. https://doi.org/10.1080/10426914.2020.1843671.

[3] Gradl PR, Protz CS, Garcia CP, Mireles OR, Leary M, Gradl PR, Protz CS, Garcia CP, Mireles OR, Leary M. Introduction to and applications of additive manufacturing for propulsion. In: Metal Additive Manufacturing for Propulsion Applications. American Institute of Aeronautics and Astronautics, Inc.; 2022. p. 1–48. https://doi.org/10.2514/5.9781624106279.0001.0048.

[4] Choudhury IA, El-Baradie MA. Machinability of nickel-base super alloys: a general review. J Mater Process Technol 1998;77:278–84. https://doi.org/10.1016/S0924-0136(97)00429-9.

[5] Gradl PR, Protz CS, Wammen T. Additive manufacturing and hot-fire testing of liquid rocket channel Wall nozzles using blown powder directed energy deposition Inconel 625 and JBK-75 alloys. In: AIAA Propulsion and Energy 2019 Forum. Indianapolis, IN: American Institute of Aeronautics and Astronautics; 2019. https://doi.org/10.2514/6.2019-4362.

[6] Liu R, Wang Z, Sparks T, Liou F, Newkirk J. Aerospace applications of laser additive manufacturing. Laser Additive Manufacturing, Elsevier 2017:351–71. https://doi.org/10.1016/B978-0-08-100433-3.00013-0.

[7] Sanchez S, Smith P, Xu Z, Gaspard G, Hyde CJ, Wits WW, et al. Powder bed fusion of nickel-based superalloys: a review. Int J Mach Tools Manuf 2021;165:103729. https://doi.org/10.1016/j.ijmachtools.2021.103729.

[8] Rodrigues TA, Malfeito A, Farias FWC, Duarte V, Lopes J, Cruz Payão Filho JD, et al. Grain refinement of Inconel 625 during wire-based directed energy deposition additive manufacturing by in-situ added TiB2 particles: process development, microstructure evolution and mechanical characterization. Intermetallics 2024;175:108540. https://doi.org/10.1016/j.intermet.2024.108540.

[9] Farias FWC, Duarte VR, Filho JDCP, Figueiredo AR, Schell N, Maawad E, et al. High-performance Ni-based superalloy 718 fabricated via arc plasma directed energy deposition: effect of post-deposition heat treatments on microstructure and mechanical properties. Addit Manuf 2024;88:104252. https://doi.org/10.1016/j.addma.2024.104252.

[10] Farias FWC, Dos Santos TJG, Oliveira JP. Directed energy deposition + mechanical interlayer deformation additive manufacturing: a state-of-the-art literature review. Int J Adv Manuf Technol 2024;131:999–1038. https://doi.org/10.1007/s00170-024-13126-5.

[11] Dupont JN, Lippold JC, Kiser SD. Solid-solution strengthened Ni-base alloys. Welding metallurgy and Weldability of Nickel-Base alloys. John Wiley & Sons, Ltd; 2009. p. 47–156. https://doi.org/10.1002/9780470500262.ch3.

[12] DuPont JN, Lippold JC, Kiser SD. Precipitation-strengthened Ni-base alloys. Welding metallurgy and Weldability of Nickel-Base alloys. 1st ed. Wiley; 2009. p. 157–254. https://doi.org/10.1002/9780470500262.

[13] Maguire MC, Michael JR. Weldability of alloy 718, 625 and variants. Superalloys 718, 625, 706 and Various Derivatives. In: The Minerals, Metals & Materials Society; 1994. p. 881–92. https://doi.org/10.7449/1994/Superalloys_1994_881_892.

[14] Lippold JC, Sowards JW, Murray GM, Alexandrov BT, Ramirez AJ. Weld solidification cracking in solid-solution strengthened Ni-base filler metals. In: Hot cracking phenomena in welds II. Springer; 2008. p. 147–70. https://doi.org/10.1007/978-3-540-78628-3_9.

[15] Caron JL, Sowards JW. Weldability of nickel-base alloys. Comprehensive Materials Processing, Elsevier 2014:151–79. https://doi.org/10.1016/B978-0-08-096532-1.00615-4.

[16] Andersson J, Jacobsson J, Brederholm A, Hänninen H. Improved understanding of varestraint testing—Nickel-based superalloys. In: Boellinghaus T, Lippold JC, Cross CE, editors. Cracking phenomena in welds IV. Cham: Springer International Publishing; 2016. p. 25–36. https://doi.org/10.1007/978-3-319-28434-7_2.

[17] Singh S, Andersson J. Hot cracking in cast alloy 718. Sci Technol Weld Join 2018;23:568–74. https://doi.org/10.1080/13621718.2018.1429238.

[18] Singh S, Andersson J. Varestraint weldability testing of cast ATI® 718Plus™—a comparison to cast alloy 718. Welding in the World 2019;63:389–99. https://doi.org/10.1007/s40194-018-0626-2.

[19] Xia C, Kou S. Evaluating susceptibility of Ni-base alloys to solidification cracking by transverse-motion weldability test. Sci Technol Weld Join 2020;25:690–7. https://doi.org/10.1080/13621718.2020.1802897.

[20] Santos GE, Miná ÉM, Pequeno DAC, De Miranda HC, Silva CC. Evaluation of solidification cracking of Ni-based alloy dissimilar welds based on trans-varestraint test. Welding in the World 2021;65:1969–82. https://doi.org/10.1007/s40194-021-01147-7.

[21] Ariaseta A, Andersson J, Ojo O. A comparative evaluation of hot cracking susceptibility of new Ni-based superalloy G27 and alloy 718. J Alloys Compd 2025;1012:178512. https://doi.org/10.1016/j.jallcom.2025.178512.

[22] Raza T, Andersson J, Svensson L-E. Varestraint weldability testing of additive manufactured alloy 718. Sci Technol Weld Join 2018;23:606–11. https://doi.org/10.1080/13621718.2018.1437338.

[23] Raza T, Hurtig K, Asala G, Andersson J, Svensson LE, Ojo OA. Influence of heat treatments on heat affected zone cracking of gas tungsten arc welded additive manufactured alloy 718. Metals 2019;9:881. https://doi.org/10.3390/met9080881.

[24] Raza T, Andersson J, Svensson L-E. Varestraint testing of selective laser additive manufactured alloy 718—influence of grain orientation. Metals 2019;9:1113. https://doi.org/10.3390/met9101113.

[25] Hosseini E, Popovich VA. A review of mechanical properties of additively manufactured Inconel 718. Addit Manuf 2019;30:100877. https://doi.org/10.1016/j.addma.2019.100877.

[26] Gonzales DS, Liu S, Javernick D, Pacheco R, Brand M, Johnson M, et al. Oxygen effects on solidification behavior of gas tungsten arc–welded laser powder bed fusion–fabricated 304L stainless steel. Materials Performance and Characterization 2019;8:20180115. https://doi.org/10.1520/MPC20180115.

[27] Deng P, Karadge M, Rebak RB, Gupta VK, Prorok BC, Lou X. The origin and formation of oxygen inclusions in austenitic stainless steels manufactured by laser powder bed fusion. Addit Manuf 2020;35:101334. https://doi.org/10.1016/j.addma.2020.101334.

[28] Faes K, Nunes R, Probst F, Ceuppens R, De Waele W. Weldability of additively manufactured powder bed fusion 316L stainless steel using arc and laser welding. Crystals 2024;14:303. https://doi.org/10.3390/cryst14040303.

[29] Guzman J, Riffel KC, Berkson JW, Casto S, Ramirez AJ. Transverse varestraint weldability testing in laser powder bed fusion 316L stainless steel. Weld World 2025. https://doi.org/10.1007/s40194-025-01933-7.

[30] Cieslak MJ, Headley TJ, Romig AD, Kollie T. A melting and solidification study of alloy 625. Metall Trans A 1988;19:2319–31. https://doi.org/10.1007/BF02645056.

[31] DuPont JN, Marder AR, Notis MR, Robino CV. Solidification of Nb-bearing superalloys: part II. Pseudoternary solidification surfaces. Metall Mater Trans A 1998;29:2797–806. https://doi.org/10.1007/s11661-998-0320-x.

[32] DuPont JN, Notis MR, Marder AR, Robino CV, Michael JR. Solidification of Nb-bearing superalloys: part I. Reaction sequences. Metall Mater Trans A 1998;29:2785–96. https://doi.org/10.1007/s11661-998-0319-3.

[33] DuPont JN, Robino CV. The influence of Nb and C on the solidification microstructures of Fe-Ni-Cr alloys. Scr Mater 1999;41:449–54. https://doi.org/10.1016/S1359-6462(99)00102-5.

[34] Savage WF, Lundin CD. The varestraint test. Weld J 1965;44. 433s–42s.

[35] Kou S. A criterion for cracking during solidification. Acta Mater 2015;88:366–74. https://doi.org/10.1016/j.actamat.2015.01.034.

[36] Soysal T, Kou S. A simple test for assessing solidification cracking susceptibility and checking validity of susceptibility prediction. Acta Mater 2018;143:181–97.

[37] Giorjao R, Sutton B, Ramirez A. New composition based technique for solidification cracking resistance evaluation. Metall Mater Trans A 2021;52:2512–21. https://doi.org/10.1007/s11661-021-06244-2.

[38] Riffel KC, Marques IJ, Leon-Henao H, Ramirez AJ, McCracken S, Tatman J. Computational approach to predict solidification cracking susceptibility in welding filler metals. Bonita Springs, Florida, USA; 2024. p. 924–32. https://doi.org/10.31399/asm.cp.am-epri-2024p0924.

[39] Hasani N, Dharmendra C, Sanjari M, Fazeli F, Amirkhiz BS, Pirgazi H, et al. Laser powder bed fused Inconel 718 in stress-relieved and solution heat-treated conditions. Mater Charact 2021;181:111499. https://doi.org/10.1016/j.matchar.2021.111499.

[40] Tajyar A, Brooks N, Holtham N, Rowe R, Newell DJ, Palazotto AN, et al. Effects of a modified heat-treatment on microstructure and mechanical properties of additively manufactured Inconel 718. Mater Sci Eng A 2022;838:142770. https://doi.org/10.1016/j.msea.2022.142770.

[41] Dupont JN, Lippold JC, Kiser SD, Weldability testing.. Welding metallurgy and Weldability of Nickel-Base alloys. John Wiley & Sons, Ltd; 2009. p. 379–402. https://doi.org/10.1002/9780470500262.ch8.

[42] American Welding Society. B4.0:2016: Standard methods for mechanical testing of welds 2016.

[43] Schindelin J, Arganda-Carreras I, Frise E, Kaynig V, Longair M, Pietzsch T, et al. Fiji: an open-source platform for biological-image analysis. Nat Methods 2012;9:676–82. https://doi.org/10.1038/nmeth.2019.

[44] ASTM International. E112–24: Test methods for determining average grain size. 2024. https://doi.org/10.1520/E0112-24.

[45] Lingenfelter A. Welding of Inconel alloy 718: a historical overview. Superalloys 718 metallurgy and applications. TMS 1989:673–83. https://doi.org/10.7449/1989/Superalloys_1989_673_683.

[46] Lingenfelter AC. Varestraint testing of nickel alloys. Weld J 1972;51:430s–6s.

[47] Arata Y, Matsuda F, Saruwatari S. Varestraint test for solidification crack susceptibility in weld metal of austenitic stainless steels. Trans JWRI 1974;3:79–88. https://doi.org/10.18910/3695.

[48] Shankar V, Gill TPS, Mannan SL, Sundaresan S. Solidification cracking in austenitic stainless steel welds. Sadhana 2003;28:359–82. https://doi.org/10.1007/BF02706438.

[49] ASTM International. Standard specification for additive manufacturing nickel alloy (UNS N06625) with powder bed fusion. 2021. https://doi.org/10.1520/F3056-14E01.

[50] Lu S, Fujii H, Nogi K. Marangoni convection and weld shape variations in Ar–O2 and Ar–CO2 shielded GTA welding. Mater Sci Eng A 2004;380:290–7. https://doi.org/10.1016/j.msea.2004.05.057.

[51] Hooijmans JW, Ouden GD. The influence of oxygen on nitrogen absorption during arc melting of iron. Welding Research Supplement; 1992.

[52] Lu S-P, Fujii H, Nogi K. Weld shape comparison with iron oxide flux and Ar–O2 shielding gas in gas tungsten arc welding. Sci Technol Weld Join 2004;9:272–6. https://doi.org/10.1179/136217104225012346.

[53] Lu S, Fujii H, Nogi K. Influence of welding parameters and shielding gas composition on GTA weld shape. ISIJ Int 2005;45:66–70. https://doi.org/10.2355/isijinternational.45.66.

[54] Lu S, Fujii H, Nogi K. Effect of welding parameters on GTA weld shape for pure iron plate under Ar-O2 mixed shielding. J Mater Sci Technol 2006;22.
[55] Yang J, Schlenger LM, Nasab MH, Van Petegem S, Marone F, Logé RE, et al. Experimental quantification of inward Marangoni convection and its impact on keyhole threshold in laser powder bed fusion of stainless steel. Addit Manuf 2024; 84:104092. https://doi.org/10.1016/j.addma.2024.104092.
[56] Sayyar N, Shamanian M, Niroumand B. Arc weldability of Incoloy 825 to AISI 321 stainless steel welds. J Mater Process Technol 2018;262:562–70. https://doi.org/10.1016/j.jmatprotec.2018.07.020.
[57] Woo I, Nishimoto K, Tanaka K, Shirai M. Effect of grain size on heat affected zone cracking susceptibility.Study of weldability of Inconel 718 cast alloy (2nd report). Weld Int 2000;14:514–22. https://doi.org/10.1080/09507110009549223.
[58] Thompson RG, Cassimus JJ, Mayo DE, Dobbs JR. The relationship between grain size and microfissuring in alloy. Weld J 1985;64. 91s–6s.
[59] Sylwestrowicz W, Hall EO. The deformation and ageing of mild steel. Proc Phys Soc B 1951;64:495–502. https://doi.org/10.1088/0370-1301/64/6/305.
[60] Petch NJ. The cleavage strength of polycrystals. J Iron Steel Res Int 1953;174:25–8.
[61] Cordero ZC, Knight BE, Schuh CA. Six decades of the Hall–Petch effect – a survey of grain-size strengthening studies on pure metals. Int Mater Rev 2016;61:495–512. https://doi.org/10.1080/09506608.2016.1191808.